THE SOLAR FLARE SOFT X-RAY DIFFERENTIAL EMISSION MEASURE AND THE NEUPERT EFFECT AT DIFFERENT TEMPERATURES

James. M. McTiernan, George H. Fisher and Peng Li

Space Sciences Laboratory University of California, Berkeley

Received ______________________; accepted ______________________

ABSTRACT

Data from the Yohkoh Soft X-ray Telescope (SXT) and Bragg Crystal Spectrometer (BCS) are used to obtain the Differential Emission Measure (DEM) of solar flare soft X-ray plasma. The Maximum Entropy Method is used to obtain the DEM for 80 flares observed by SXT and BCS from October, 1991 to November, 1992. We find that it is often difficult to describe the DEM using a monotonically decreasing function; functions with a hump at high temperature are occasionally more useful. From the time history of the DEM, we show that higher temperature plasma peaks earlier and cools faster. We also show that the high temperature plasma ($>$ 16.5 MK) is more likely than low temperature plasma to exhibit the so-called "Neupert effect", in which the time derivative of the soft X-ray emission measure is similar to the light curve of the impulsive hard X-ray emission for the flare.

Subject headings: Sun: Flares, Sun: X-rays, gamma-rays

1. Introduction

For thermal sources such as the soft X-ray plasma in solar flares, the amount of hot material is given by the Emission Measure, defined as

$$EM = \int n^2 dV \tag{1}$$

where n is the plasma density and V the volume of the emitting plasma, for an isothermal source.

From observations, we know that the solar flare soft X-ray plasma is not isothermal. The value of temperature, T, measured using the isothermal assumption always depends on the energy bandpass of the detector used. This is demonstrated in Figure 1, which shows temperatures measured by the Yohkoh SXT and BCS for a flare which occurred on 5 November, 1992. For all flares, BCS measures a higher value of T than SXT, because the BCS detector sees shorter wavelength, higher energy emission (1.8 to 5 A, in four channels) than the SXT detector (3 to 20 A, multiple filters); it is more sensitive to high temperature plasma than SXT. (Culhane et al. 1991, Tsuneta et al. 1991). Consequently, when interpreting observations, and comparing results with models, it is necessary to know the response of the observing instrument.

For a multitemperature plasma, the Differential Emission Measure (DEM), $q(T)$, is an indication of how much hot material there is as a function of temperature, or

$$EM = \int \frac{d(n^2V)}{dT} dT = \int q(T) dT \quad , \tag{2}$$

where EM now represents the emission measure integrated over all temperatures.

The DEM describes the thermal emission from the flare plasma, in a way that in principle does not depend on the bandpass of a given detector. In this work, we will use data from two different detectors, the Yohkoh Soft X-ray Telescope (SXT; Tsuneta et al. 1991) and Bragg Crystal Spectrometer (BCS; Culhane et al. 1991) to obtain the soft X-ray DEM.

The Yohkoh SXT has a spatial resolution of 2.5 arcsec and is sensitive to relatively low temperature (3 to 20 MK) plasma. The SXT observes flares with 5 different broad-band filters, which gives it the ability to estimate the plasma temperature and emission measure using filter ratios (McTiernan et al. 1993). As shown in Tsuneta et al. (1991), it is difficult to use the SXT alone in deriving the DEM distribution due to the extremely broad, overlapping temperature responses for the different filters.

The Yohkoh BCS observes flares in four channels, observing lines of S XV (5.01 to 5.11 A), Ca XIX (3.16 to 3.19 A), Fe XXV (1.83 to 1.89 A) and Fe XXVI (1.76 to 1.80 A). These are designed to obtain temperature and emission measure in the range from 10 to 50 MK. With the combination of the SXT and BCS, we can cover the range from 3 to 50 MK.

Our use of BCS differs from previous uses; past studies of BCS data have concentrated on obtaining diagnostics using the good spectral resolution of BCS in the individual channels. Here, the BCS is treated as a broad-band detector; the line photon flux in each BCS channel is summed and that data is treated in the same way as the SXT data. All information about the plasma motion is lost, since motion affects the line shape and position within the channel, but we gain the ability to estimate the DEM, which until now has not been done using Yohkoh data. (Note that the emission from moving plasma is still included in the calculation; mass motion does not affect the total number of photons emitted in the line.) The SXT data is summed over its own spatial resolution (the SXT images used are partial frame 64×64 flare-mode images), since BCS is a full-Sun instrument.

There has never been a study of the DEM distribution for a large sample of solar flares. Some work has been done regarding the solar flare DEM in the past, from work with Solrad and Skylab data (Dere & Cook 1979), through the SMM era (Sylwester, Schrijver & Mewe

1980; Jakimiec et al. 1984; Gabriel et al. 1984; Strong et al. 1986), but these studies covered only a small sample of events. Recent DEM determinations have been done mostly using EUV (EUVE) and X-ray (ASCA) observations of quiet stars and stellar flares, with very little solar work done (Del Zanna et al. 1996; Monsignori-Fossi et al. 1996; Mewe et al. 1996, 1997; Cully et al. 1997).

Other calculations have used Yohkoh BCS data to find the Velocity Differential Emission Measure, or VDEM, which gives the amount of flare plasma as a function of fluid velocity, but not as a function of temperature (Newton, Emslie & Mariska, 1995, 1996). We make no determination of velocity, so the work described here should be considered to be complimentary to that of Newton, Emslie & Mariska.

We have a number of objectives for this study. The DEM is one of the few observationally inferred quantities that can be directly compared with theoretical models. Flare heating models, which predict temperature, pressure and density as functions of space and time, also predict the DEM. For different flare heating mechanisms, the models may produce different results. There have been many hydrodynamic models of flares, e.g., Antiochos & Sturrock (1976, 1978); Antiochos & Krall (1979); Nagai & Emslie (1984); Emslie (1985); Fisher, Canfield & McClymont (1985 a,b,c); Mariska, Emslie & Li (1989); Serio et al. (1991); Jakimiec et al. (1992); Emslie, Li & Mariska (1992); and Li, Emslie & Mariska (1993). Since there are few recent DEM reconstructions derived from observations, authors rarely show their theoretical DEM. In the above list of references, only Emslie (1985) and Mariska, Emslie & Li (1989) actually include plots of the DEM as a function of temperature. To compare with observations, it is necessary to reduce the model DEM down to single temperature results (Sylwester et al. 1993; Antonucci & Martin 1995; Reale et al. 1997).

We also would like to examine the so-called "Neupert effect" as it applies to the behavior of plasma at different temperatures. It is well known that the soft X-ray time derivative is similar to the hard X-ray (or microwave) light curve (Neupert 1968; Dennis & Zarro 1993). This is known as the "Neupert effect". It has been shown in theoretical work (e.g., Li, Emslie & Mariska 1993) that this effect can be reproduced if the flare energy release occurs in the form of nonthermal electrons. The nonthermal electrons lose their energy via Coulomb collisions in the lower corona and upper part of the chromosphere. The temperature rises and a high pressure region forms which drives material both upward and downward (chromospheric evaporation and chromospheric condensation). The coronal temperature and density are enhanced as the evaporated material rises, resulting in increased soft X-ray emission.

In this case the hard X-ray light curves are proportional to the time profile of the accelerated electrons. The soft X-ray emission, which is emitted from the plasma heated by the nonthermal electrons, is proportional to the accumulated energy deposited by the electrons up to a given time, even when losses due to thermal conduction and mass motion are considered. The soft X-ray emission is thus proportional to the time integral of the profile of the input electrons, and we therefore expect the Neupert effect between soft and hard X-rays. Note that the small impulsive soft X-ray loop footpoint sources that have been observed in some SXT flares are not accounted for by this model (Hudson et al. 1994; McTiernan et al. 1993; Li, McTiernan & Emslie 1997).

If we know how the DEM behaves with respect to the hard X-ray electrons, we can place constraints on flare models, whether they involve chromospheric evaporation by HXR electrons or other heating mechanisms. In particular we can show how the plasma exhibits the Neupert effect, and whether this effect takes place in the high temperature plasma, the low temperature plasma, or in all of the plasma.

We can also use the DEM to study the behavior of the plasma after the HXR burst, to see if there is an extended period of heating beyond that expected from the hard X-ray light curve. The DEM gives us a much better tool for studying the evolution of the soft X-ray plasma energy than does the isothermal approximation (although it is still limited, as discussed later). If energy in the soft X-ray plasma continues to increase beyond the end of the hard X-ray burst, then additional heating is needed.

2. Data Analysis

For these calculations we use data from the Al.1 (1400 Åthick Aluminum), Al12 (12μ thick Aluminum) and Be119 (119μ thick Beryllium) filters of SXT, and the Ca XIX and Fe XXV channels of BCS. All of the line flux in the Ca XIX channel is included in the fit, including any due to moving plasma. Bulk motion can cause the line profile to be blue-shifted or red-shifted, but this has no effect on our analysis unless the shifts are large enough to drive the photon flux out of the channel, a situation that does not occur for any of the flares in our sample. A sample BCS Ca XIX channel spectrum is shown in the top panel of Figure 2.

The middle and bottom panels show sample spectra for the Fe XXV channel, where the situation is more difficult; in many cases the line profile can be shifted enough so that photons in the complex of lines on the right are not detected; this is shown in the middle panel. In other cases the line profile is shifted to the left, in which case there may be extra photons. This is shown in the bottom panel. These shifts in the Fe XXV channel are due not to plasma motion, but instead to the design of the instrument; the wavelength of a line that is actually observed by BCS has some dependence on the position of the flare, since it depends on the angle of the of the incident photons relative to the BCS crystal (Bragg angle, see Culhane et al. 1991). This also happens for the Ca XIX channel, but the effect on the total line flux is negligible, since there is no line emission near the channel edges.

To avoid the problems caused by the line complex on the right of the Fe XXV range, we only use the part of the channel that includes the Fe XXV resonance line, i.e., the part of the spectrum to the left of the vertical line in the plots. Note that this vertical line is chosen for a given flare by averaging the minimum point between the resonance line and the line complex for all of the spectra of the flare. This quantity is constant during flares; for the 13 January 1992 flare the observed wavelength at the minimum is $1.857 \pm 0.003 \AA$.

A plot of the temperature responses for the different channels/filters is shown in Figure 3. The BCS responses are obtained using the IDL program BCS_SPEC, which is distributed as part of the Yohkoh software package. The solar coronal abundances used in the Yohkoh SXT and BCS software are adopted from Meyer (1985).

3. TEST DATA

To model the DEM, we divide the temperature range into four bins and assign an emission measure to each bin. The amount of emission measure in the bins is then varied to minimize χ^2. We use four bins since we have five data points; the minimization routine used, AMOEBA (Numerical Recipes, Press, et al. 1986), is not stable unless there are fewer bins than data points.

This histogram-DEM fits the data well, often resulting in reduced χ^2 values which approach unity; for example, the average reduced χ^2 value for histogram-DEM fits for the 5 November 1992 flare shown in Figure 1 is 2.5. We improve the solution by using the histogram-DEM as the starting point for a Maximum Entropy Method (MEM) calculation. (The MEM algorithm is the same as that used for Yohkoh HXT images, see Sakao 1994.) The MEM calculation does not converge unless its starting point is very close to the final answer; thus the good starting point given by the histogram-DEM is absolutely necessary.

(For a review of DEM calculations using different methods, including MEM, see Fludra & Sylwester 1986.)

Note that the units of the DEM in this paper are $EM/(10^{47}\mathrm{cm}^{-3}\mathrm{MK})$, so that the total emission measure is the integral of the DEM over T, not $\ln(T)$.

Some sample test calculations are shown in Figure 4. For the test calculations, an initial DEM is assumed, and integrated over the temperature responses. This is used as input to a Monte Carlo calculation in which a large number of data sets are generated from the original by randomly varying each data point by an amount of up to 2%. (This value was chosen because typical uncertainties in the actual data are of the order of 2%.) We then obtain a DEM from each data set, and average the results to obtain the final DEM. The uncertainty for the final DEM at each temperature is given by its standard deviation. The top panel of Figure 4 shows the results for a DEM which is a decreasing power law in temperature, a model DEM with which we have had some success in previous work (McTiernan 1996). The solid curve shows the initial DEM, the dashed line shows the histogram-DEM, and the solid histogram with error bars shows the final DEM, which is very close to the initial test DEM. Note that the deviations between the initial and final DEM are the largest at the lowest temperatures (2-4 MK). This is because there is very little temperature response in any of the filter or channel bandpasses at low T. Thus the lowest T DEM can vary by a large amount and still have only a small effect on the observed data.

In the middle panel of Figure 4 we test the model using a two-component DEM, in this case a power law T dependence with a broad hump with a peak at 20 MK. Again, the test results fit the original distribution well.

In the bottom panel, we test the model using a DEM obtained from loop model calculations of Fisher & Hawley (1990). The model is for a "static" loop, in which the heating and cooling of the flaring loop takes place slowly enough so that loop scaling laws are obeyed at all times. Fisher & Hawley studied flare loops in three limiting cases, "strong evaporation", "static", and "strongly condensing". For each case the DEM has a sharp cusp at the loop apex temperature, which is also the maximum temperature. For the evaporation case, the DEM varies as $T^{-1/2}$ below the cusp, for the static loop the DEM is constant below the cusp, and the condensing loop model has a DEM that is proportional to T below the cusp.

The loop model shown in the bottom panel of Figure 4 has the high-temperature cusp, but the calculation does not return the cusp shape, instead returning a broad hump. The peak of the hump in the "observed" DEM is 3 MK below the original cusp, with some emission measure existing at temperatures above the original peak. This is due to the lack of good temperature resolution; there is no good way to distinguish temperature structures of less than a few MK. It is not due to the assumed uncertainties. To try to reproduce the cusp, the calculation was done with no random variation of the data in each filter/channel. The resulting DEM still has a broad hump. This DEM solution has a reduced χ^2 value of 0.0003, and each data point is within 0.01% of the initial value. Beyond this point, the MEM solution oscillates; the cusp cannot be reproduced.

4. RESULTS

The DEM inversion analysis described above was carried out for 92 flares which occurred between October, 1991 and November, 1992. For a number of flares, no model fit the data particularly well; in some cases it is obvious that there is a source seen by BCS that is not present in the SXT data. This happens when SXT is observing a flare at one location, and another flare occurs at a different position. In flare mode, SXT does not shift its observing region to observe the new flare; thus, SXT does not see all of the emission that BCS does, since BCS observes the entire Sun. In other cases, there are different data gaps for the two different instruments which are too large for interpolation. For the rest of the flares that did not fit well, the flux in the Fe XXV channel was always seriously underestimated by the model; for these cases, either there was a high temperature component that was missed or the Fe XXV response is incorrect. This could be due to abundance variations or ionization non-equilibrium effects — if the Fe XXV ion is over abundant, there will be more counts in the channel. We will return to these events on an individual basis in the future.

Note that by "a good fit" we mean a reduced χ^2 value of less than or close to unity. In practice, a "good fit" means that the photon fluxes in each channel/filter are within one or two percent of the observed data, for the entire flare. The uncertainties in the SXT data are a combination of photon counting statistics, subtraction of the CCD dark current, scattering by the neutral density (ND) filter used to increase the SXT dynamic range, and data compression/uncompression. It turns out that the uncertainty due to Poisson statistics for the large number of photons involved in the SXT filters (which can be as high as 10^6 or 10^7 per filter) are small, and are often smaller than the uncertainties due to the other sources. This is different from the situation for spatially resolved SXT images, for which Poisson uncertainties dominate (McTiernan et al. 1993). The total SXT uncertainties are typically of the order of 1%; for example, the flare shown in Figure 1, of 5 November 1992 the uncertainty in the Be119 filter data ranges from 0.9% to 1.7%.

The uncertainties for BCS channels are relatively larger than those for SXT, typically ranging from 1% to 5%. This includes the Poisson uncertainties in the line photon flux and the continuum flux. The continuum flux is subtracted from the total photon flux in each channel to obtain the total line photon flux. (The number of photons per BCS data point typically ranges from 10^2 to a few times 10^4 per channel). A 1% systematic uncertainty is added to the data for both SXT and BCS to account for the possibility of unknown factors, such as calibration or abundance uncertainties.

The uncertainties are propagated through the entire calculation. The uncertainties for the MEM-DEM are calculated using a routine developed for Yohkoh HXT images developed by Metcalf et al. (1996). In calculations for which there is no standard error propagation formula (e.g., the calculation of peak times for curves and derivatives), the Monte Carlo method, as described in the discussion of the test data, was used.

The final sample contains 80 flares; DEM distributions were derived with 9 s time resolution, for ~ 30 to ~ 100 points for each flare.

As might be expected, results for real flares do not look like model results. The DEM for flares of 13 January 1992 and 19 February 1992 is shown in Figures 5 and 6. In each Figure, the DEM is shown at four different times. In each plot the dash-dot line is the histogram-DEM, in four temperature bins, and the solid line is the MEM-DEM. For each flare, the four plots correspond to: a) the first available BCS data interval (the accumulation time for the intervals is 9 s) b) a point during the rise phase, c) the BCS-Fe XXV channel maximum; d) the SXT-Al.1 maximum.

Our loop models typically have a DEM that increases with T, as we have discussed, and the flares have DEMs that decrease with T. The exception to this is the strong evaporation model, for which there is a $T^{-1/2}$ dependence at low temperatures, but also a cusp at the apex temperature. If the loop models are correct, we would expect to see a hump near the maximum temperature, and a relatively low, flat DEM for low temperatures, as in the bottom panel of Figure 4. This would be true even in the case of strong evaporation for which the DEM decreases by only a factor of 2 between 5 and 15 MK. Instead we see a large low T component with either a long high T tail, or a relatively small high T hump. If we fit a power law to the decreasing part of the low temperature component for the DEMs shown in Figures 5 and 6, we find that the power law index ranges from -1.0 to -2.5, much larger than the -0.5 expected in the strong evaporation limit.

There is another way to show that the loop models do not agree with the data. We can simply take the loop model DEM, integrate over the temperature responses, and compare to the observed count rates in SXT and BCS. For example, the loop model used in the bottom panel of Figure 4 results in a ratio of Ca XIX counts to Al.1 counts of 0.0015. In our sample of 80 flares, this ratio reaches a value that high once, for 72 s of a flare which occurred on 18 December, 1991. For most flares, the Ca XIX/Al.1 ratio is a factor of 3 smaller (0.0005 ± 0.0002). If the cusp is moved to a lower temperature, 13 MK, to account for the low Ca XIX/Al.1 ratio, then there is no response in the Fe XXV resonance line; the resulting Fe XXV/Al.1 counts ratio is 2.0×10^{-5}. This low a value for the Fe XXV/Al.1 ratio is seen for 5 of the 80 flares in the sample, at the very end of each flare, so a low-temperature cusp is possible, but only at the very end of a few flares.

Note that the models of Emslie (1985), and Mariska, Emslie & Li (1989), which return differential emission measures that increase with temperature, are also not consistent with this data.

4.1. Two Components

For the 13 January 1992 flare, (Masuda et al. 1994) there is a distinct high temperature hump in the DEM. Nine of the 80 flares in the sample show high temperature humps with peak values which are at least twice the height of the minimum DEM between the hump and the low T component. Typically the minimum between the two components is reached in the 10 to 15 MK range, and the peak of the hump is in the range 18 to 27 MK. There is no correlation between this behavior and flare size or position. (See Table 1.) The 13

January flare is unique in that it has the largest hump, with a peak high T DEM that reaches 1/3 of the value of the low T DEM.

Note that the hump is necessary for these cases. We have attempted to fit the results with monotonically decreasing functions (single and broken power law fits, with high T cutoffs), and these do not fit the data. For example, in the time range for which the hump is prominent for the 13 January 1992 flare, the best monotonically decreasing power law and broken power law fits to the data have reduced χ^2 values between 4 and 8, while for the histogram and MEM DEM, for the entire flare, $\chi^2 \lesssim 1$. Both the histogram DEM and the broken power law fits are four parameter fits, with five data points, and therefore one degree of freedom. The probability of occurrence for the histogram DEM fits is $\gtrsim 0.3$, and that for the broken power law fits ranges from 0.005 to 0.05 during the time when the hump is noticeable.

Note that early in the flare, and at the end of the flare, when the hump is not there, the power law, broken power law, histogram and MEM all give $\chi^2 \lesssim 1$, so the power law fits are certainly acceptable at those times. The advantage of using the MEM DEM is that it can exhibit the behavior of both the monotonically decreasing DEM and the hump DEM.

When the high temperature hump is present, the results look very much like results obtained from SMM data for a flare of 8 April 1980 by Strong et al. (1986). The high T component appears during the rise phase, then increases in emission measure, while decreasing in temperature, until it merges with the low T component. The behavior is qualitatively similar for the cases which do not show a distinct high T hump. The high T DEM is an extended tail on the low T DEM. This tail is more prominent early in the flare and it eventually merges with the low T component as the flare cools.

4.2. Thermal Energy, High versus Low Temperatures

The high T DEM can account for a substantial amount of energy, even though it is small relative to the DEM at low T. If we assume that the pressure, P, inside the emitting volume, V, is uniform (Strong et al. 1986), then the total thermal energy $(3/2)PV$ is

$$E_{th} = 3kV^{1/2}\sqrt{\int_0^\infty T^2 q(T)\, dT}\ . \tag{3}$$

For the sake of comparison, we divide the energy range into two regimes, separated by a critical temperature, $T_c = 16.5$ MK, so that "high T" plasma has $T \geq T_c$ and "low T" plasma has $T < T_c$. If we assume that, in addition to spatially uniform pressure, the total volume of the soft X-ray flare plasma does not change with time, we find

$$E_{lo} = 3kV^{1/2}\left(\int_0^\infty T^2 q(T)\, dT\right)^{-1/2} \int_0^{T_c} T^2 q(T)\, dT \tag{4}$$

for the thermal energy of the low T plasma, and

$$E_{hi} = 3kV^{1/2}\left(\int_0^\infty T^2 q(T)\, dT\right)^{-1/2} \int_{T_c}^{\infty} T^2 q(T)\, dT \tag{5}$$

for the thermal energy of the high T plasma.

These quantities are plotted for the 13 January 1992 flare in the top panel of Figure 7, for the energy in the low and high temperature ranges, and the total energy.

Since the rest of this paper will often refer to comparisons between the "low" and "high" temperature ranges, the seemingly arbitrary choice of 16.5 MK as the dividing line between these ranges should be justified. This value was chosen after an inspection of the data showed that the time of the peak value of the high T thermal energy, and the times of peaks of the derivative of the high T energy are close to the same times for the counts in the Fe XXV resonance line. (This is true for all of the flares, not only the 13 January 1992 flare.) In Figure 3, the response of the Fe XXV line is at 10% of its peak value at 16.5 MK.

Thus when we refer to "high T" plasma, we are referring to the plasma that causes most of the response in the Fe XXV line. All of the rest is "low T" plasma. It should be noted that we obtain nearly the same results for our comparisons using a value for T_c anywhere in the range of 15 to 20 MK.

As can be seen from Figure 7, the high T thermal energy peaks earlier and cools faster. An original motivation for this study was to see how the plasma cooling time varies as a function of T. For the 13 January 1992 flare the e-folding energy loss time is 330 s for the high T plasma. The BCS flare-mode observations did not last long enough for us to get a reasonable cooling time for the low T component (this is true for most of the flares in the study). Instead, since there is very little high T plasma left late in the flare, we assume that all of the plasma seen by SXT is low temperature, and we use SXT Al.1/Al12 observations to obtain the energy loss time. In this way we find a cooling time of 1890 s for the low T component. If we define α as the ratio of high T to low T cooling times, we find $\alpha = 0.17$.

If a plasma cools by heat conduction, then the cooling time for a plasma decreases with increasing temperature; the conductive cooling time is $\tau_c \propto T^{-5/2}$. If the plasma cools by radiation, then the cooling time increases with increasing T; $\tau_r \propto T^{3/2}$. (This expression for τ_r is valid if the slope of the radiative loss function for high T is -0.5; Cargill, Mariska & Antiochos 1995.) Our results are not directly comparable to these cooling times, since the cooling times are calculated by assuming an isothermal plasma with a temperature that varies with time, and we calculate the decay time of the energy in the plasma in different temperature ranges. The plasma in the interval $q(T)dT$ at one time is not necessarily the same as the plasma in the same interval at a later time.

We can, nevertheless, guess that the fact that the cooling time decreases with increasing T indicates that conduction plays a role in the cooling of the thermal plasma. Whether conduction dominates at all temperatures is not clear. Models which have the appropriate

DEM distributions need to be found, and the cooling times must be calculated from those models for comparisons.

4.3. The Neupert Effect For High and Low Temperatures

The bottom panel of Figure 7 shows a comparison of the time derivatives of the low T, high T and total plasma energy with the count rate in 33-93 keV hard X-rays as seen by the Yohkoh HXT. The data is smoothed over 27 s time resolution to smooth fluctuations in the data before the derivative is calculated. The high T derivative peaks at the same time as the hard X-rays, and drops to zero when the hard X-rays drop to the background level. This is a clear example of the Neupert effect.

The low T derivative is not similar to the HXT curve at all. It remains positive for seven minutes after the HXT burst. The increase in low T plasma energy after the HXT burst looks as if it is due to cooling of the high T plasma; the low T component is relatively constant up until the end of the HXT burst, and then increases as the high T component decreases. Note that the low T plasma energy is greater than the high T plasma energy at the start of the flare, thus all of the energy does not initially go into the high T plasma.

The total energy derivative peaks at the same time as the hard X-rays, but it remains positive until two minutes after the HXT burst. The peak in the total energy time profile is broad, and in fact the maximum energy could occur anywhere from one to three minutes after the burst. The energy increase after the HXT emission is gone indicates that there may be another heating source besides nonthermal electrons, but given the uncertainty in the total energy peak position, we cannot say this for sure.

Once the DEM behavior is understood, it is easy to explain the time variations seen in the SXT and BCS data. The top plot of Figure 8 shows the data from the Al.1 (line) and

Be119 (line with pluses) filters of SXT, and the Fe XXV channel of BCS (stars), for the same flare. The bottom plot shows the time derivatives of the same data, along with the HXT data. For this case, the curves have been arbitrarily scaled. The Fe XXV channel is mostly sensitive to high T plasma, and its derivative closely matches the hard X-ray time profile. The Be119 filter is sensitive to both low and high T plasma; its derivative has a peak with the HXT burst, and remains positive long after the HXT burst. The Al.1 filter is sensitive to high and low T plasma, but is much more sensitive to low T plasma than the Be119 filter. Its derivative has a peak with the HXT burst, but also has a peak long after the HXT burst. The Al.1 brightness increases (i.e., has a positive derivative) until 17:37 UT. The late increase in Al.1 counts is not due to extra heating, however; the total energy decreases after 17:32 UT. Instead, it is due to cooling of the high T plasma, and the corresponding increase in low T plasma. The plasma moves into the temperature range where the Al.1 filter is more sensitive, and the Al.1 brightness increases, even though the total energy in the plasma is decreasing.

Our point is that a knowledge of the DEM is necessary before one can interpret the Neupert effect and determine whether there is extended heating beyond that due to nonthermal electrons. If, for example, only SXT data are included, then it is easily shown that heating lasts for a long time after the HXT burst, and that the Neupert effect is not necessarily present. If only BCS data are included then the Neupert effect is obvious and heating ends with the hard X-ray burst. In reality, the answer may be somewhere in between.

The 13 January 1992 flare is typical in the way it shows the Neupert effect, but all flares do not necessarily behave in the same way. Figure 9 has the same format as Figure 7, for a flare occurring on 19 February 1992. Here, the soft X-ray derivatives do not look like the HXT time profile, and they all remain positive after the HXT emission returns to the background level. The derivative of the high T component and the total energy have peaks just before and 1 minute after the HXT peak. The second peak occurs after the end of the HXT burst. The low T component derivative has a small peak at the point where the HXT burst peaks, and a higher peak later in the flare, long after the HXT burst. The behavior of the low and high T components relative to each other is similar to the 13-Jan-1992 flare, but their relation to the HXT time profile is different.

Consistence or non-consistence with the Neupert effect was determined by an automated procedure that correlates positive soft X-ray derivatives with HXR emission above the background level. For each flare, in each temperature range, a Neupert "score" is calculated as follows: for each time interval, the soft X-ray and hard X-ray light curves are compared. For a given interval, if the soft X-ray time derivative and the hard X-ray count rate have the same sign (i.e., if both are positive, or if both are negative or zero) then one is added to the score. If the signs of the soft X-ray time derivative and the hard X-ray counts are opposite, then one is subtracted. The score is then divided by the total number of time intervals. Flares with scores which are close to 1.0 (in a possible range from -1.0 to 1.0) can be considered to be consistent with the Neupert effect. Flares with low scores are not consistent with the Neupert effect.

For example, the Neupert scores for the 13-jan-1992 flare are 0.95 ± 0.03, -0.02 ± 0.09, and 0.75 ± 0.08, for the high T energy, low T energy, and the total energy, respectively. The high T plasma energy and total energy are consistent with the Neupert effect, as can be seen from Figure 7. The scores for the 19-Feb-1992 flare are 0.30 ± 0.07, -0.38 ± 0.07, and 0.16 ± 0.03. The uncertainties for each flare were calculated using a Monte Carlo method in which the SXR energy and HXR count rate were varied randomly, by an amount up to their uncertainties. This was done for a large number of trial data sets; the final score for a given flare is the average of the scores for the trial data sets, and the uncertainty in the score is the standard deviation of the set of trial scores.

5. The Full Sample

Results for the entire sample of 80 flares are shown in Table 1. For each flare, the table shows: the date, the peak time of the Fe XXV emission, the GOES X-ray class, the flare position on the disk from SXT, the time lag between the peak of the high T energy and the peak of the low T energy (i.e., the low T peak time minus the high T peak time), α (the ratio of the low T decay time to the high T decay time), whether or not there is a high temperature hump in the DEM at any point for the flare, and whether or not the emission is consistent with the Neupert effect in the high T range, the low T range and for the total energy.

From the table we find that the low T peak occurs after the high T peak for all but one flare. For 63 of the 65 flares for which we were able to calculate decay times for both the low T and high T components, the ratio α is less than 1. It is clear that the high temperature plasma ($>$ 16.5MK) peaks earlier and decays faster than the low temperature plasma. This is a characteristic of conductive cooling, as mentioned previously, but a combination of conductive and radiative cooling cannot be ruled out.

Only 9 of the flares had a high temperature hump in the DEM. These humps are always smaller than the low T DEM. (Here we have defined a "hump" as follows: the DEM decreases to a minimum, then increases with increasing T to a peak value that is more than twice the size of the aforementioned minimum.) This does not rule out the possibility of plasmas with two separate components for the rest of the flares, it simply means that any separate high T component is not large enough for us to resolve with our limited temperature resolution. There is no correlation between the presence of high T humps and flare size or position, but we should note that most of the flares in this sample are in a limited size range, from high C-class to low M-class. We could not analyze larger flares because BCS saturates for large flares. Large flares may indeed have relatively larger high T components, since the average temperature for flares increases with flare size (Feldman et al. 1996). There is no way for us to make that determination.

There are 33 flares in the sample which have a peak HXT background subtracted count rate of greater than 100 counts/s in the energy range above 33 keV, and no large data gaps, for which we can make the Neupert effect comparison. At high temperature, these flares neatly divide into two groups; there are 24 flares that have Neupert scores of greater than 0.60, and can be said to be consistent with the Neupert effect, and 9 flares that have scores of less than 0.42, and are not consistent. There are no borderline cases. To test whether 24 of 33 flares is a significant correlation, we do the same comparison, except in this case each soft X-ray light curve is compared with a random hard X-ray curve drawn from the same sample. This is repeated a number of times in yet another Monte Carlo calculation. From the random sample, for high T emission, we would expect $15(\pm 2)$ flares to have a score greater than 0.60, so the number of flares which show consistence with the Neupert effect in the original sample is greater than would arise from random chance. For low temperature radiation, only 3 of the 33 flares are consistent with the Neupert effect, $5(\pm 2)$ would be expected from a random sample. For total plasma energy, 14 of the 33 flares are consistent with the Neupert effect, $10(\pm 2)$ would be expected from a random sample.

We conclude that the Neupert effect is a high T phenomenon. High temperature plasma, such as that observed by the Yohkoh BCS Fe XXV channel, typically shows the Neupert effect. Low temperature plasma, which dominates the radiation seen by the Yohkoh SXT, rarely shows this property. One cannot use this last fact to argue that the soft X-ray emission is not due to heating by energetic electrons, however. The low temperature plasma energy may be increasing later in the flare simply because high temperature plasma is cooling and becoming low temperature plasma itself. When we look at the total energy in the SXR plasma, we find that approximately one-half (14 of 33) of the flares exhibit the Neupert effect. For the other 19 flares, an additional heating mechanism is indicated.

These results are similar to those reported by Dennis & Zarro (1993), who compared the position of the peaks of the soft X-ray derivative to the peaks of the hard X-ray light curve to determine whether flares were consistent with the Neupert effect. Our method is different, but the results are similar. Dennis & Zarro found that 80% of the flares in their sample showed the Neupert effect. They used the GOES soft X-ray detector in their study; the GOES detector is more sensitive to high T plasma than the SXT, so one would expect a good level of consistency with the Neupert effect.

It is important to note that the determination of the energy in the different temperature ranges is the result of a rather simple calculation. A more accurate calculation, involving the calculation of the spatially resolved DEM, is clearly necessary. Some ideas of the spatially resolved DEM can be gleaned from close examination of SXT images, by comparison of different filter ratios, and this will be done in future work. The HESSI mission will give imaging and spectroscopic observations of flares for energies down to 3 keV. This will give us images of the high T plasma continuum emission and the Fe line complex, and can be used for DEM calculations in conjunction with Yohkoh, SXI, or possibly Solar-B data.

6. CONCLUSIONS

The main conclusions that should be drawn from this work are:

(1) The solar flare soft X-ray plasma is not isothermal. DEMs for solar flares can be obtained using SXT and BCS data.

(2) In the temperature range to which the SXT and BCS are sensitive, the DEM typically decreases with increasing T; some flares show humps in the high T DEM, but these are smaller than the low T DEM. This is not what we expect from loop models, for which the DEM increases with T, or decreases gradually, before increasing to a high T cusp.

(3) Even though the DEM is smaller for high T, there can be a substantial amount of energy in the high T plasma. It should be noted, however, that not all of the energy initially goes into the high T component, since the low T component is nonzero at the start of the flare.

(4) Higher temperature plasma peaks earlier and cools faster, as is shown for the flares in the sample in Table 1. This is a characteristic of conductive cooling.

(5) The Neupert effect is noticeable at high T for almost all of the flares. Roughly one-half of the flares show this effect when considering the total energy, under the assumption that the total volume occupied by the soft X-ray emitting plasma remains constant during the flare. Low T plasma is rarely consistent with the Neupert effect.

The authors would like to thank U. Feldman and B. Dennis for useful comments and discussions. This work was supported by NASA grant NAGW-5126 and Lockheed subcontract LMSC-SA30G4740R.

REFERENCES

Antiochos, S.K. & Sturrock, P.A. 1976, Solar Phys., 49, 359

Antiochos, S.K. & Sturrock, P.A. 1978, Ap. J., 220, 1137

Antiochos, S.K. & Krall, K.R. 1979, Ap. J., 229, 788

Antonucci, E. & Martin, R. 1995, Ap. J., 451, 402

Cargill, P. J., Mariska, J. T. & Antiochos, S. K. 1995, Ap. J., 439 1034

Culhane, J.L. et al. 1991, Solar Phys., 136, 89

Cully, S.L., et al. 1997, Ap. J., 491, 910

Del Zanna, G. et al. 1996, in Cool, Stars, Stellar Systems, and the Sun: Ninth Cambridge Workshop, Florence, Italy, 3-6 Oct. 1995. Astronomical Society of the Pacific Conference Series, 109, 259

Dennis, B.R. & Zarro, D.M. 1993, Solar Phys., 146, 177

Dere, K.P. & Cook, J.W., Ap. J., 229, 772

Emslie, A.G. 1985, Solar Phys., 98, 281

Emslie, A.G., Li, P. & Mariska, J.T. 1992, Ap. J., 399, 714

Feldman, U., et al. 1996, Ap. J., 460, 1034

Fisher, G.H., Canfield, R.C. & McClymont, A.N. 1985a, Ap. J., 289, 414

Fisher, G.H., Canfield, R.C. & McClymont, A.N. 1985b, Ap. J., 289, 425

Fisher, G.H., Canfield, R.C. & McClymont, A.N. 1985c, Ap. J., 289, 434

Fisher, G.H. & Hawley, S.L. 1990, Ap. J., 357, 243

Fludra, A. & Sylwester, J. 1986, Solar Phys., 105, 323

Gabriel, A. H. et al. 1984, Adv. Space Res., 4, No. 7, 221

Hudson, H. S. et al. 1994, Ap. J. (Letters), 422, L25

Jakimiec, J. et al. 1984, Adv. Space Res., 4, No. 7, 23

Jakimiec, J. et al. 1992, Astr. Ap., 253, 269

Li, P., Emslie, A.G. & Mariska, J.T. 1993, Ap. J., 417, 411

Li, P., McTiernan, J. M. & Emslie, A.G. 1997, Ap. J., 491, 395

Mariska, J.T., Emslie, A.G. & Li, P. 1989, Ap. J., 341, 1067

Masuda, S. et al. 1994, Nature, 371, 495

Metcalf, T. R. et al. 1996, Ap. J., 466, 585

McTiernan, J.M. et al. 1993, Ap. J. (Letters), 416, L91

McTiernan, J.M. 1996, in Magnetic Reconnection in the Solar Atmosphere: Proceedings of a Yohkoh Conference, eds. R.D. Bentley & J.T. Mariska, 228

Mewe, R. et al. 1996, in Cool, Stars, Stellar Systems, and the Sun: Ninth Cambridge Workshop, Florence, Italy, 3-6 Oct. 1995. Astronomical Society of the Pacific Conference Series, 109, 273

Mewe, R. et al. 1997, Astr. Ap., 320, 147

Meyer, J.P. 1985, Ap. J. Suppl., 57, 173

Monsignori-Fossi, B.C. et al. 1996, Ap. J., 466, 427

Nagai, F. & Emslie, A.G. 1984, Ap. J., 279, 896

Neupert, W.M. 1968, Ap. J., 153, L59

Newton, E.K., Emslie A.G. & Mariska J.T. 1995, Ap. J., 447, 915

Newton, E.K., Emslie A.G. & Mariska J.T. 1996, Ap. J., 459, 804

Press, W.M. et al. 1986, Numerical Recipes (Cambridge University Press, New York), Chapter 10

Reale, F. et al. 1997, Astr. Ap., 325, 782

Sakao, T. 1994, Ph.d. Thesis, Univ. of Tokyo

Serio, S. et al. 1991, Astr. Ap., 241, 197

Strong, K.T., et al. 1986, in Energetic Phenomena on the Sun, The Solar Maximum Mission Flare Workshop Proceedings, NASA Conference Publication 2439, Section 5.3

Sylwester, J., Schrijver, J. & Mewe, R. 1980, Solar Phys., 67, 285

Sylwester, B. et al. 1993, Astr. Ap., 267, 586

Tsuneta, S., et al. 1991, Solar Phys., 136, 37

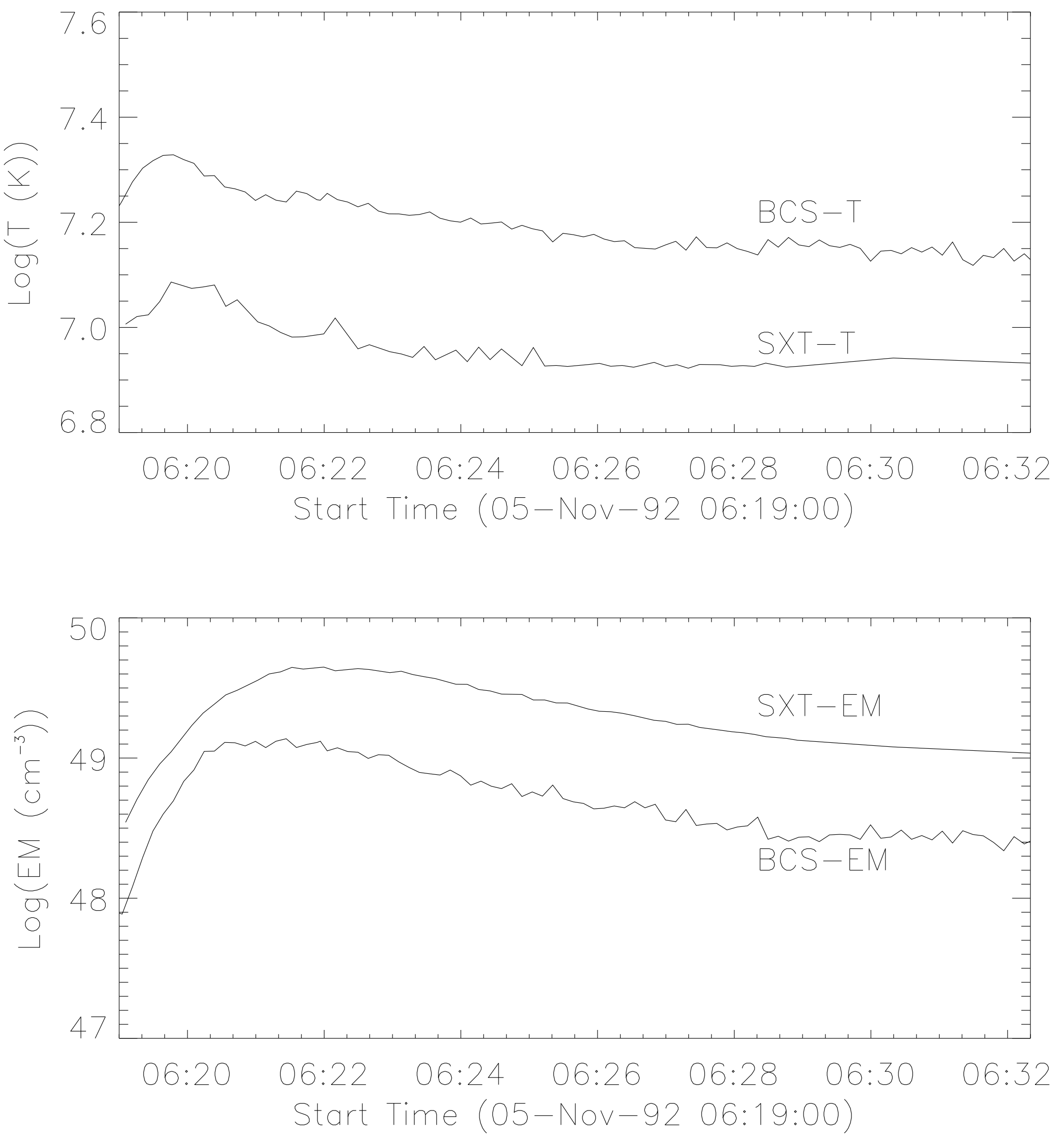

Fig. 1.— Yohkoh SXT and BCS temperature and emission measure versus time for the 5 November, 1992 flare.

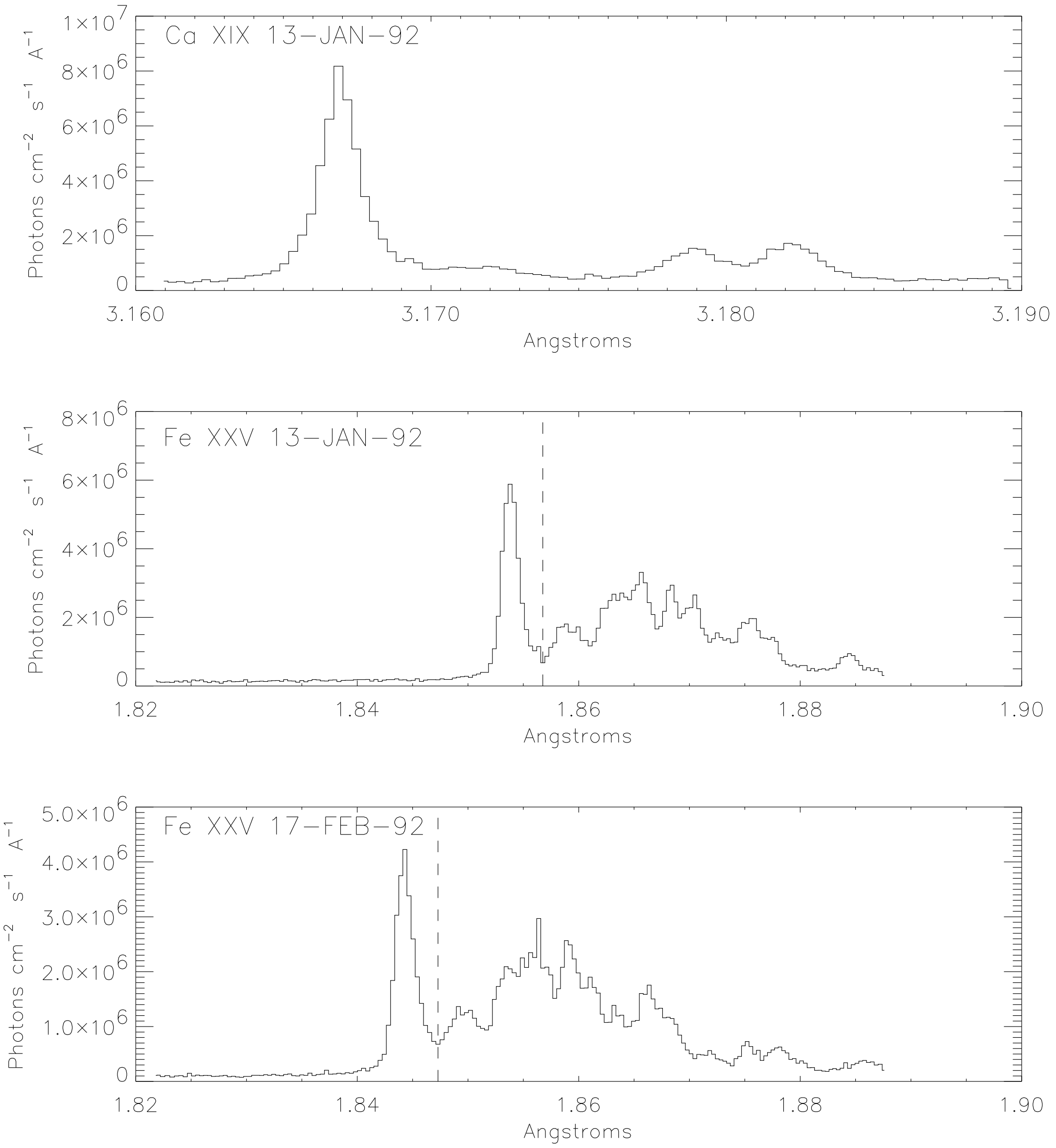

Fig. 2.— BCS spectra, Top Panel: The spectrum in the Ca XIX channel at the peak of Ca XIX emission a flare of 13 January 1992. Middle Panel: The Fe XXV channel spectrum at the peak of Fe XXV emission for the 13 January 1992 flare. Bottom Panel: The Fe XXV channel spectrum at the peak of Fe XXV emission for a flare of 17 February 1992. The nominal wavelength of the Fe XXV resonance line is 1.508 angstroms. Only the data to the left of the dashed line in the Fe XXV channel is used in our study.

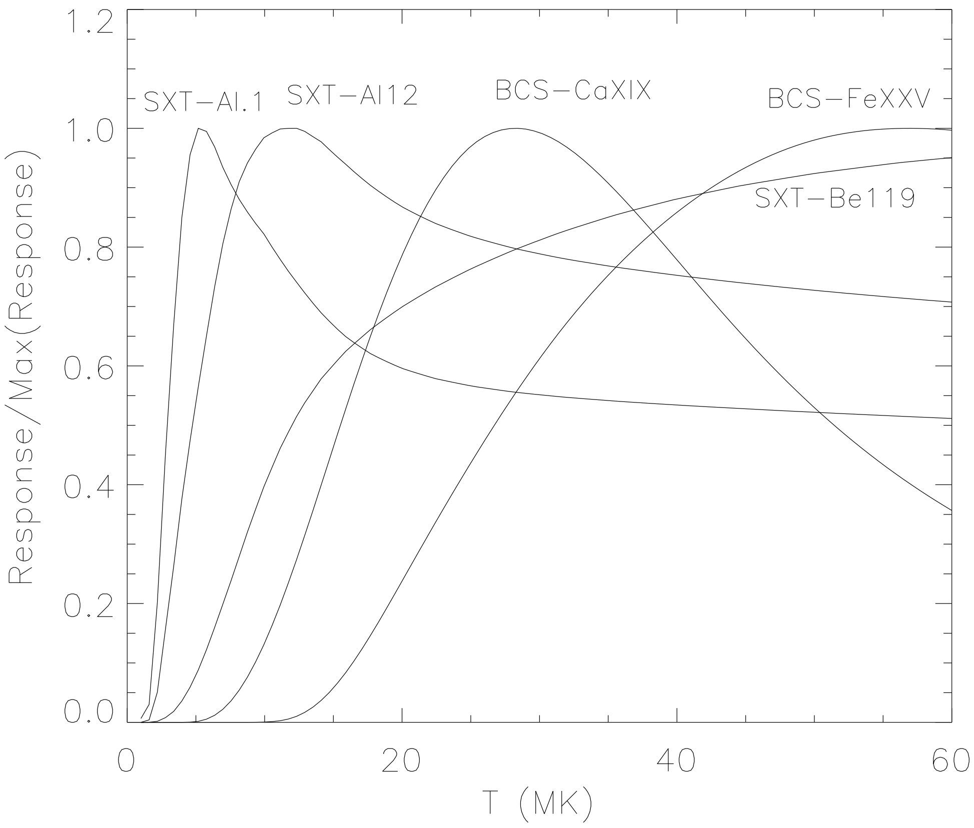

Fig. 3.— The normalized T response for the SXT filters and BCS channels used. Note that the SXT responses extend to high temperatures. Since the T responses are so broad, we do not expect to resolve features in the DEM smaller than a few MK.

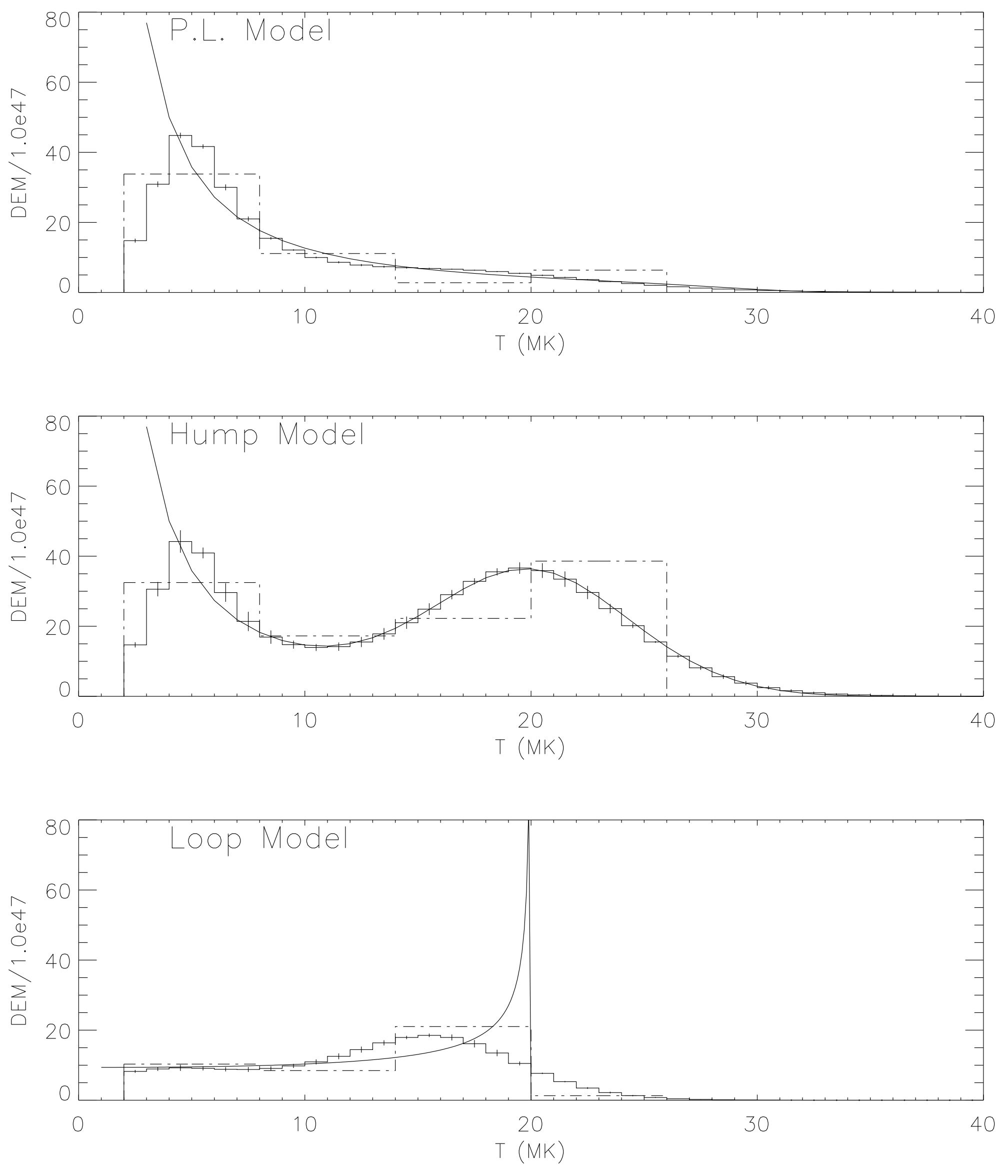

Fig. 4.— Model DEM tests: The top panel shows a DEM that is a decreasing power law in T. The solid curve is the input model DEM. The dot-dash line is a histogram fit to the model, in 4 bins. The histogram with error bars is the MEM fit to the data. In the middle panel, the model DEM is a power law plus a broad hump centered at 20 MK. In the bottom panel, a static loop model is used.

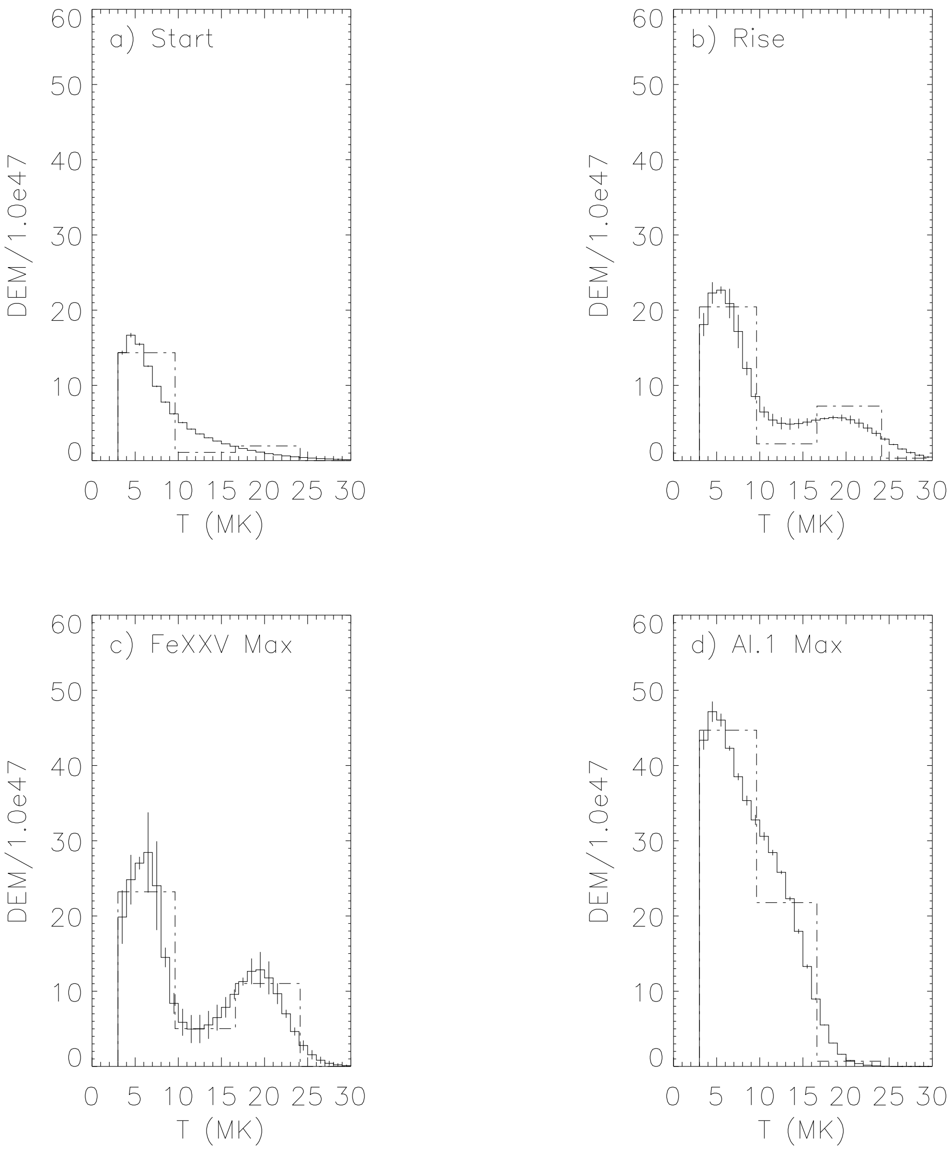

Fig. 5.— The DEM for four different times for the flare of 13 January 1992. The dash-dot line is the histogram-DEM, in four bins (in some cases only three may be visible; the fourth bin has too little emssion measure to be seen), and the solid line is the MEM-DEM.

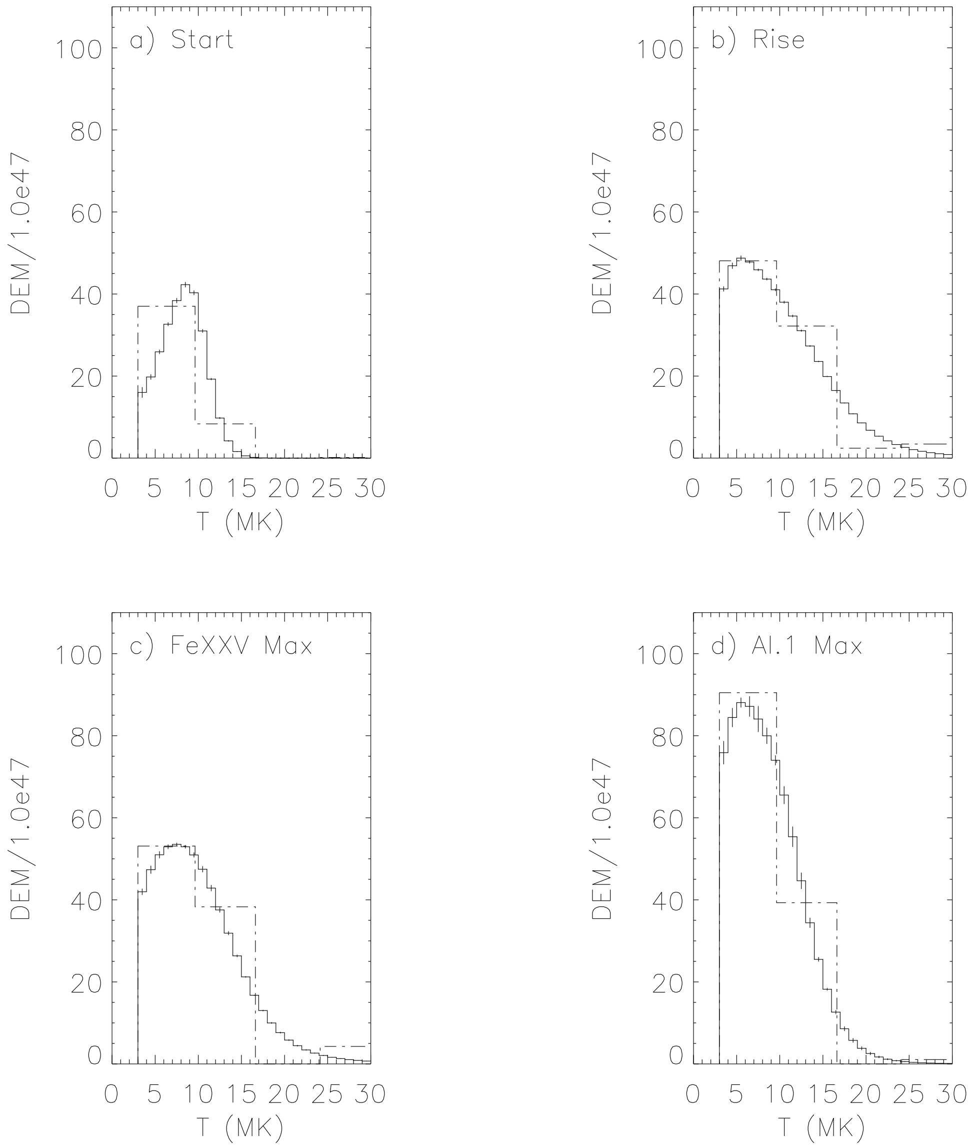

Fig. 6.— The DEM for four different times for the flare of 19 February 1992. The format is the same as in Figure 5.

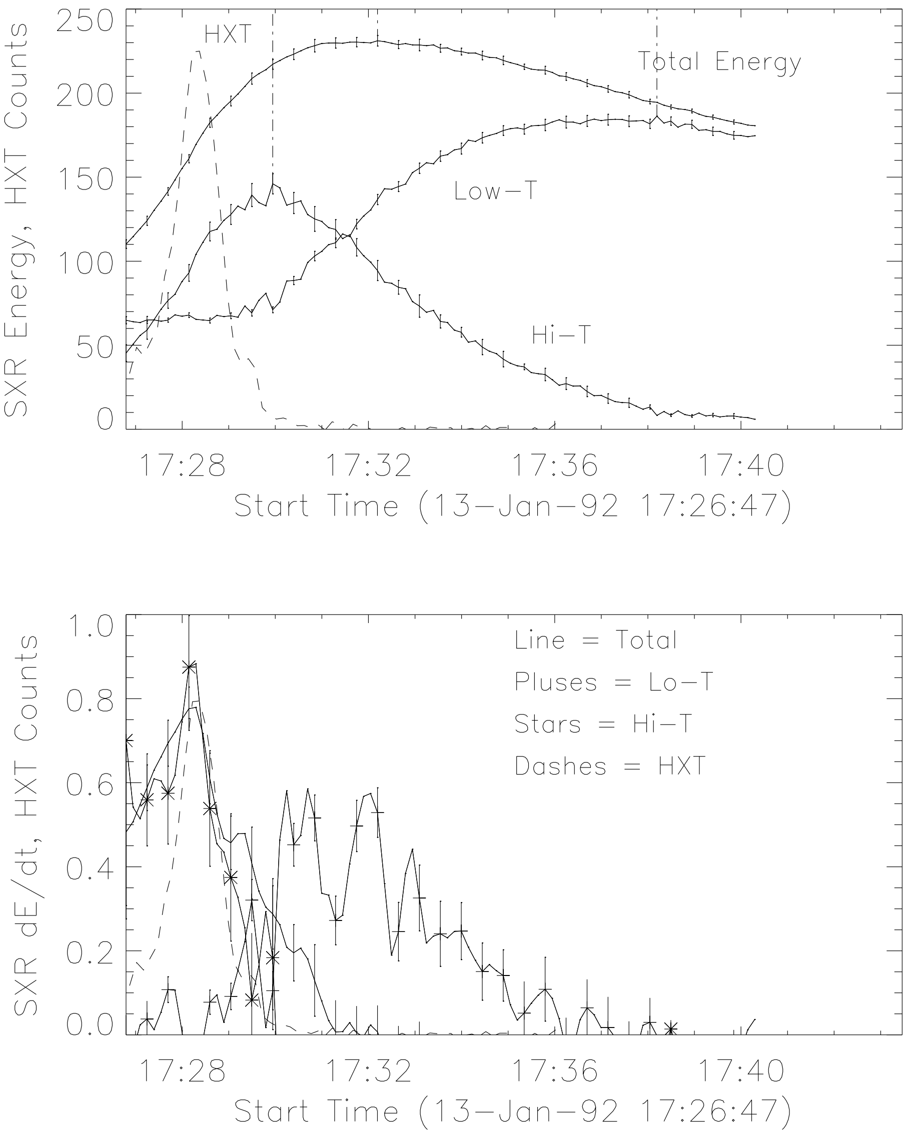

Fig. 7.— Top: The thermal energy as a function of time for the 13 January 1992 flare. The curves for total energy, low T ($<$ 16.5 MK) energy, and high T are so annotated. The HXT time profile is indicated by the dashed line. Bottom: The derivatives of the energy curves, along with the normalized HXT count rate for hard X-rays above 33 keV (dashed line). The solid line represents the total energy, the line with plus signs represents low T energy, and the line with stars represents the high T energy. Error bars are shown for every third point, 27 s apart.

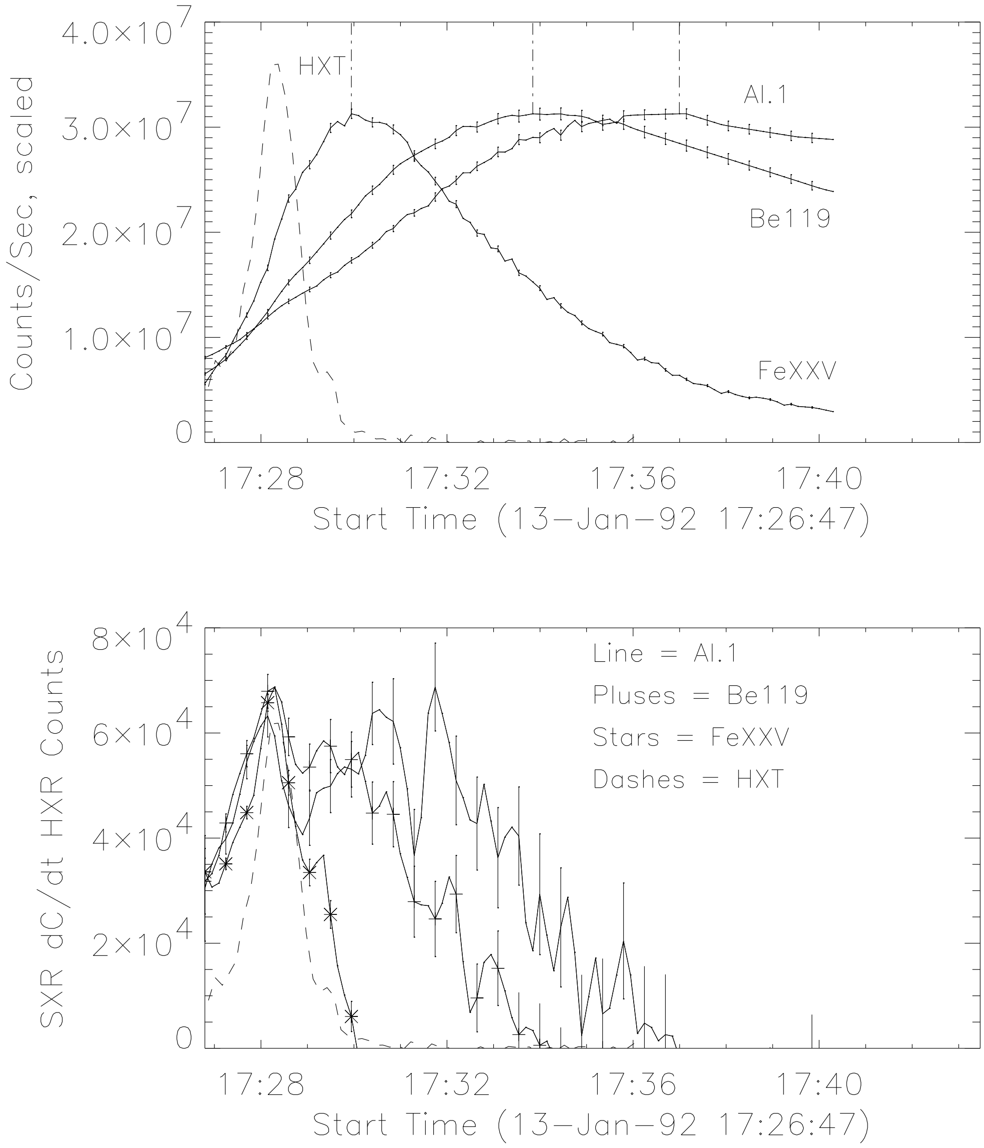

Fig. 8.— Top: SXT and BCS data for the 13 January 1992 flare. The curves for SXT Al.1 data, SXT Be119 data, BCS Fe XXV data are so annotated. The HXT time profile is indicated by the dashed line. Bottom: The derivatives of the count rates, along with the normalized HXT count rate for hard X-rays above 33 keV (dashed line). The solid line represents SXT Al.1 data, the line with plus signs represents SXT Be119 data, and the line with stars represents BCS Fe XXV data.

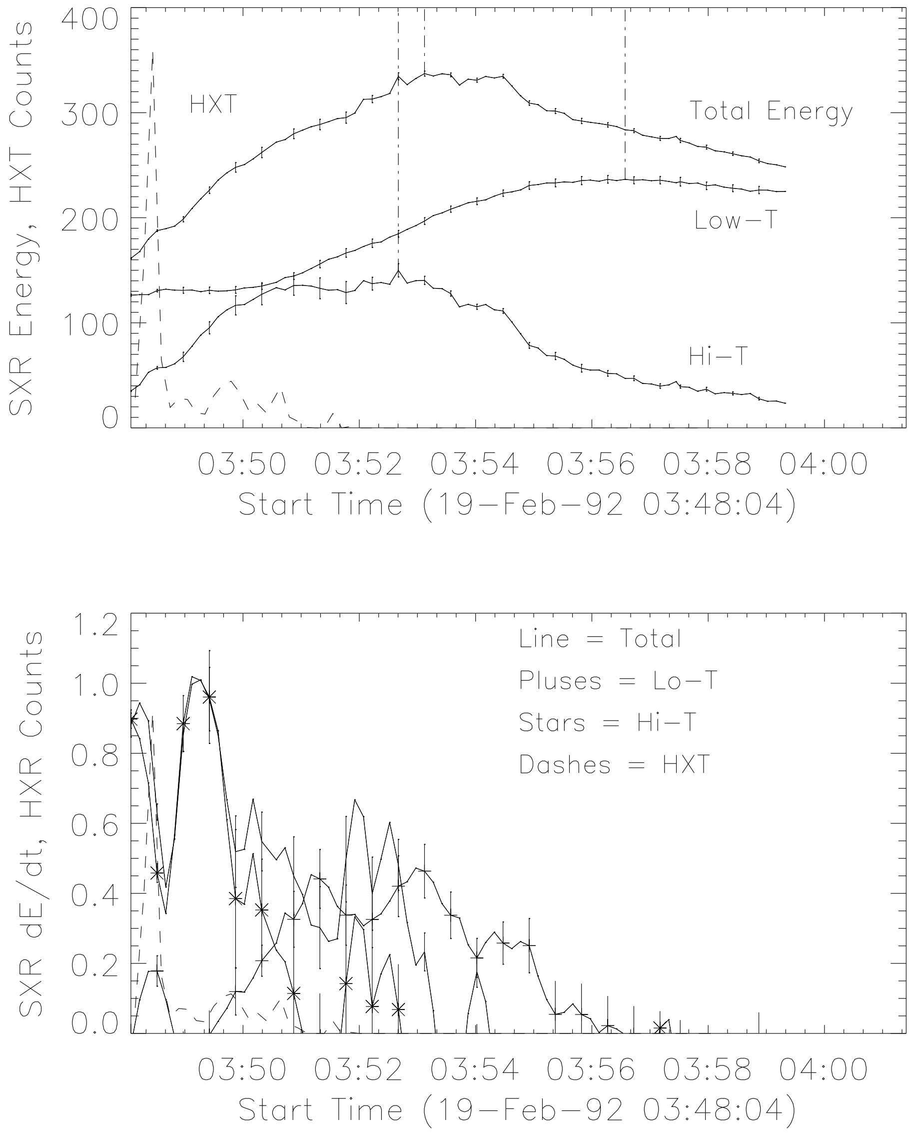

Fig. 9.— Top: The thermal energy as a function of time for the 19 February 1992 flare. The solid line represents the total energy, the line with plus signs represents the energy for low temperatures (< 16.5 MK), and the line with stars represents the energy for high temperatures. Bottom: The derivatives of the energy curves, along with the normalized HXT count rate for hard X-rays above 33 keV (dashed line).

Table 1. Flare Characteristics

Time (UT)	GOES	Pos	Time Lag (s)	α	Two Comp	Neupert Effect High T	Neupert Effect Low T	Neupert Effect Total
24-OCT-91 06:29:00	M1.2	S9E62	140	0.18	NO	YES	NO	YES
26-OCT-91 00:13:41	M1.1	S16E34	160	0.12	NO	—	—	—
28-OCT-91 01:08:58	M1.1	S13E3	476	0.09	NO	—	—	—
29-OCT-91 09:59:33	M1.2	S14W15	144	—	NO	NO	NO	NO
31-OCT-91 09:11:02	M1.0	S14W39	136	0.15	NO	YES	NO	YES
9-NOV-91 03:16:37	M1.5	N20E19	274	0.11	NO	NO	NO	NO
17-NOV-91 05:10:59	C7.7	N20W80	72	—	NO	—	—	—
17-NOV-91 18:33:31	M1.9	S13E82	59	0.20	NO	YES	NO	YES
8-DEC-91 16:03:11	M1.4	N16E12	78	—	NO	—	—	—
10-DEC-91 04:02:28	C9.3	S15E90	93	0.26	NO	—	—	—
12-DEC-91 17:06:17	M1.3	S17W29	37	0.70	NO	—	—	—
15-DEC-91 14:23:33	M1.0	N5W41	120	0.05	YES	—	—	—
16-DEC-91 03:13:58	C7.8	S12E70	73	0.29	NO	YES	NO	NO
16-DEC-91 06:39:37	M1.6	S12E67	102	0.70	NO	YES	NO	YES
16-DEC-91 22:06:12	C7.4	S12E59	56	0.17	NO	—	—	—
18-DEC-91 10:27:52	M3.5	S14E90	298	0.14	YES	—	—	—
26-DEC-91 21:41:00	M4.2	S16E19	315	0.72	NO	YES	NO	NO
5-JAN-92 13:21:11	M1.9	S12E8	198	—	NO	YES	NO	NO
7-JAN-92 04:09:29	M1.5	S15W10	401	1.35	YES	NO	NO	NO
7-JAN-92 20:24:11	C8.9	S15W20	123	0.11	NO	NO	NO	NO
13-JAN-92 17:29:56	M2.0	S16W90	436	0.17	YES	YES	NO	YES
30-JAN-92 02:30:28	M1.6	S2W1	191	0.55	NO	YES	NO	YES
30-JAN-92 13:57:13	M1.8	S14W46	125	0.32	NO	YES	NO	YES
3-FEB-92 06:59:52	M1.2	S11E29	98	0.21	NO	—	—	—
6-FEB-92 00:19:37	C9.9	N13E84	71	0.99	NO	—	—	—
7-FEB-92 11:56:26	M3.7	S18W51	163	0.79	NO	YES	YES	YES
9-FEB-92 03:02:31	M1.2	S17W76	273	0.41	NO	—	—	—
17-FEB-92 15:42:39	M1.9	N15W79	229	0.58	NO	YES	NO	NO
19-FEB-92 03:52:22	M3.7	N4E84	232	0.20	NO	NO	NO	NO
19-FEB-92 23:28:23	C7.7	N1E66	73	0.36	NO	—	—	—
26-FEB-92 01:38:14	M1.3	S15W90	95	0.17	NO	YES	NO	YES
29-FEB-92 20:42:20	M1.7	S12W26	518	0.65	NO	—	—	—
25-MAR-92 18:48:17	C7.4	N5E45	122	—	NO	—	—	—
24-APR-92 12:51:49	M1.4	N10E4	295	—	NO	—	—	—
24-APR-92 19:19:02	M1.2	N13W1	27	0.40	NO	YES	YES	YES

Table 1—Continued

Time (UT)	GOES	Pos	Time Lag (s)	α	Two Comp	Neupert Effect High T	Neupert Effect Low T	Neupert Effect Total
7-JUN-92 01:45:07	M2.7	N7E10	168	0.32	NO	YES	NO	YES
8-JUN-92 08:47:14	M1.5	N7W7	122	0.23	NO	—	—	—
23-JUN-92 10:59:38	C3.6	N10W39	331	0.47	NO	YES	NO	NO
23-JUN-92 23:22:38	C3.4	N11W45	158	0.23	NO	—	—	—
24-JUN-92 09:39:48	C2.2	N11W51	41	—	NO	—	—	—
24-JUN-92 18:53:52	C3.6	N10W57	40	0.20	NO	—	—	—
24-JUN-92 23:55:07	C3.7	N10W58	151	0.06	NO	—	—	—
25-JUN-92 18:03:46	M1.4	N10W72	826	0.27	YES	YES	NO	YES
3-JUL-92 09:52:37	M2.1	N12E28	70	—	YES	YES	NO	NO
4-JUL-92 22:49:24	C6.9	S13E89	121	0.18	NO	—	—	—
5-JUL-92 19:58:49	M1.1	S13E86	60	0.01	NO	—	—	—
11-JUL-92 15:22:57	C5.3	S14E3	388	0.57	NO	—	—	—
12-JUL-92 17:21:57	C4.2	N16W87	83	0.10	NO	—	—	—
13-JUL-92 08:04:42	C7.6	S9W4	117	0.30	NO	—	—	—
14-JUL-92 17:49:10	C6.0	S11W32	108	0.20	NO	NO	NO	NO
15-JUL-92 02:00:54	C4.2	S11W36	122	0.15	NO	YES	NO	NO
15-JUL-92 03:50:13	C5.3	S23W17	119	0.31	NO	—	—	—
16-JUL-92 01:11:39	C5.0	S12W43	144	0.19	NO	—	—	—
17-JUL-92 21:10:53	C7.1	S9W64	94	0.28	NO	YES	NO	NO
17-JUL-92 22:38:45	C5.3	S11W87	165	0.18	NO	—	—	—
18-JUL-92 01:35:48	C5.1	S14W89	155	0.26	NO	—	—	—
18-JUL-92 05:09:45	C5.8	S14W89	99	0.40	NO	—	—	—
30-JUL-92 22:34:27	NA	N19E33	85	0.47	NO	—	—	—
11-AUG-92 13:49:06	C7.2	S14W43	184	0.15	YES	YES	NO	NO
16-AUG-92 13:56:10	C2.9	N16E26	103	0.24	NO	—	—	—
17-AUG-92 23:59:52	C4.3	N19E1	9	—	NO	NO	NO	NO
18-AUG-92 13:27:37	C1.8	N18W7	45	—	NO	—	—	—
24-AUG-92 01:13:13	C2.2	N15W90	76	0.07	NO	—	—	—
24-AUG-92 06:09:31	C2.5	N16W86	159	—	NO	—	—	—
4-SEP-92 01:37:53	NA	S9W7	30	—	NO	—	—	—
7-SEP-92 08:57:10	M1.2	S11W55	257	0.05	YES	NO	NO	NO
10-SEP-92 22:54:30	M3.2	N14E44	185	0.34	NO	YES	NO	YES
11-SEP-92 06:08:38	M1.4	N15E34	64	0.27	NO	NO	NO	NO
15-SEP-92 01:59:20	C2.6	N14W79	41	—	NO	—	—	—
16-SEP-92 23:51:07	C3.7	N14W40	174	0.12	NO	—	—	—

Table 1—Continued

Time (UT)	GOES	Pos	Time Lag (s)	α	Two Comp	Neupert Effect High T	Neupert Effect Low T	Neupert Effect Total
30-SEP-92 04:52:00	C2.9	N6E25	62	—	NO	—	—	—
5-OCT-92 09:27:21	M2.0	S8W89	250	0.37	YES	YES	NO	NO
7-OCT-92 10:11:10	M1.3	S7E30	119	1.30	NO	—	—	—
12-OCT-92 21:52:12	C2.5	S16W88	72	0.05	NO	—	—	—
22-OCT-92 18:44:18	C5.1	S8E13	0	—	NO	—	—	—
22-OCT-92 20:31:16	C3.2	N3W17	107	0.19	NO	—	—	—
23-OCT-92 22:50:33	C6.6	N2W34	44	0.50	NO	—	—	—
26-OCT-92 00:52:38	C5.5	S14E56	106	0.18	NO	—	—	—
27-OCT-92 22:19:27	C5.4	N7W90	68	0.33	NO	—	—	—
5-NOV-92 06:20:22	M2.0	S18W89	138	0.08	NO	YES	YES	YES